



Application of Passive Radiative Cooling for Dew Condensation

Daniel Beysens, Marc Muselli, Irène Milimouk, Catherine Ohayon, Simon Berkowicz, Emmanuel Soyeux, Marina Mileta, Pascal Ortega

► To cite this version:

Daniel Beysens, Marc Muselli, Irène Milimouk, Catherine Ohayon, Simon Berkowicz, et al.. Application of Passive Radiative Cooling for Dew Condensation. *Energy Journal*, 2006, 31 (13), pp.2303-2315. hal-00164933

HAL Id: hal-00164933

<https://hal.science/hal-00164933v1>

Submitted on 10 Mar 2023

HAL is a multi-disciplinary open access archive for the deposit and dissemination of scientific research documents, whether they are published or not. The documents may come from teaching and research institutions in France or abroad, or from public or private research centers.

L'archive ouverte pluridisciplinaire **HAL**, est destinée au dépôt et à la diffusion de documents scientifiques de niveau recherche, publiés ou non, émanant des établissements d'enseignement et de recherche français ou étrangers, des laboratoires publics ou privés.



Distributed under a Creative Commons Attribution - NonCommercial 4.0 International License

Radiative cooling for dew condensation

Joachim Trosseille^{a,*}, Anne Mongruel^a, Laurent Royon^b, Daniel Beysens^{a,c}

^a*Physique et Mécanique des Milieux Hétérogènes, CNRS, ESPCI Paris - PSL University,
Sorbonne Université, Sorbonne Paris Cité, 75005, Paris, France*

^b*Laboratoire des Energies de Demain, Sorbonne Paris Cité, UMR 8236CNRS, 75013,
Paris, France*

^c*OPUR, 2 rue Verderet, 75016 Paris, France*

Abstract

We describe a radiative cooling chamber which reproduces in the laboratory radiative cooling and subsequent dew formation. Based on radiative exchange with a cold source (at a temperature of nearly -80 °C), which acts as a cold black body, cooling power of at least 50 W.m⁻² is achieved. Radiative exchange is quantitatively estimated. This original device permits to study under controlled air temperature and humidity the formation of dew on any system (material, biological) for which contact cooling is inefficient, and in particular investigate the influence of radiative and wetting surface properties on dew yield. It is applicable to the study of dew itself and its effects on plants and small animals, as well as dew atmospheric chemistry, and more generally of any natural radiative cooling application.

Keywords: Dew, Condensation, Radiative cooling, Emissivity, Infrared

2010 MSC: 00-01, 99-00

1. Introduction

Atmospheric humidity can be condensed in the form of dew on a surface radiatively cooled below the air dew point temperature. The dew point defines the temperature at which air is saturated with water vapor, *i.e* water vapor

*Corresponding author

Email address: joachim.trosseille@espci.fr (Joachim Trosseille)

contained in air is at saturation pressure. Radiative cooling of the surface is obtained overnight by a deficit between the emitted radiation from the surface and the radiation coming from the atmosphere. In the context of global warming and decrease of pure water resources, dew water can be seen as a non-conventional source of water, giving an appreciable amount of good quality water to population and animals living in places where water is lacking. Dew can have a positive role for plants, bringing nocturnal moisture, especially in arid areas or during droughts (but also a negative action, favouring the development of fungal diseases). Dew also takes part in the chemistry of atmosphere, for instance in the nitrites oxides diurnal (and nocturnal) cycle. For a general review, see [1, 2]. Regarding the typical value of radiative loss for nocturnal conditions where dew forms ($\approx 60 \text{ W.m}^{-2}$), the upper thermodynamic limit of dew yield is around $0.7 \text{ litre/m}^2/\text{night}$ [1, 2, 3, 4].

On natural surfaces, dew always occurs as dropwise condensation, following different stages from the heterogeneous nucleation of a single droplet, its growth by incorporation of water vapor molecules and its interactions with neighboring droplets by coalescences [2]. Dew collection is achieved passively by gravity provided that water droplets have reached a typical size enabling them to easily slide down the surface to be collected at the surface lower edge. The quest for enhancing and controlling droplet shedding has motivated a considerable amount of experimental investigations focusing on the wetting properties of the surfaces, with the development of complex hierarchical micro-structures often inspired by natural surfaces [2].

However, all these laboratory experiments are performed by conductive (contact) cooling of thin objects (sheets, plates, wafers ...). In this arrangement, the bottom surface of the object is in thermal contact with a cooling device (*e.g.* a Peltier stage). For given thermal losses, decreasing the temperature of the upper surface of the object below the dew point temperature is a process that is thus limited by the thermal resistance of the object (the ratio of its thickness to its surface area and thermal conductivity). In outdoor devices, the dew collector is usually isolated from below and its upper surface is cooled by radiative deficit

with the atmosphere. Hence, the upper surface temperature does not depend on the thermal conductivity of the dew collector, but on its surface emissivity and on the heat exchange coefficient with the surrounding air. For such reason, radiative cooling proves more efficient for objects with high thermal resistance to heat conduction. This includes complex 3D geometries such as plant leaves, cactus spines, insect shells, spider nets, etc ...

Outdoor experiments on radiative cooling surfaces for dew collection have been widely performed since the 90's [4, 5, 6, 7]. Here, we aim to develop their indoor counterpart, with the idea of getting rid of the outdoor disadvantages (weather variations, duration and cost of experiments). To our knowledge, indoor radiative devices have received very little attention, except more than 50 years ago and nearly exclusively from biologists. Several prototypes have been developed in order to simulate the effect of radiative dew or frost on various plants (fruits, eucalyptus leaves, strawberry leaves, potatoes ...). Pioneering works used a nitrogen atmosphere in a chamber [8], or boiling nitrogen pulverized on a surface [9, 10, 11]. Several chambers were developed thereafter on the same concept, but using refrigeration devices [12]. Moreover, precautions were taken to separate the cold source from the rest of the chamber by films transparent to infrared radiation, and to prevent water condensation on those films [13, 14, 15, 16, 17]. More recently, a dew simulation chamber (Mercia Scientific, UK), based on the prototype of [12] was used to quantify the amount of dew formed on artificial sea-grass [18]. In all the above-mentioned radiative chambers, no quantitative evaluation has been carried out of their performances in terms of homogeneity and radiative cooling power. Note that an indoor device has been reported very recently in a study with radiative cooling power similar to what is found under outdoor conditions [19]. However this device, designed only for daytime cooling, does not provide the humid air conditions needed to generate condensation.

It is thus the aim of this article to present an original device developed to reproduce the phenomenon of radiative dew in the laboratory and to obtain quantitative data on the dynamic of the physical process. Based on radiative

exchange with a cold source, cooling power of at least 50 W.m^{-2} is achieved in order to reproduce the main features of natural dew formation under controlled conditions. It permits to study, among other phenomena, the influence of radiative and wetting properties of surfaces on dew harvesting in a controlled humidity and temperature environment.

2. Materials and method

The experimental setup needs to meet some basic requirements in order to simulate natural dew. First, the condensation surface (also denoted as "dew collector") has to be exposed to an exclusively radiative thermal deficit. In addition, the condensation surface has to be surrounded by humid air with controlled temperature and relative humidity. A high content of water vapor in the air is needed to reproduce the nocturnal air conditions. Finally, in order to collect quantitative data, it is necessary to measure the temperature of air and dew collector, together with the mass of condensed water. Figure 1 shows a schematic view of the experimental setup designed to meet the above specifications.

The device consists in a cylindrical chamber (4) with 10 cm height and 8 cm internal diameter. Cooling is performed by a cold source (1) at a temperature of 194.7 K located under the setup. The dew collector (2) is placed on a sample holder (3), positioned inside the cylindrical chamber (4) and resting on a balance (5). Humid air is injected from the top of the chamber, and evacuated at the bottom. The flux is measured and controlled by the flowmeter (10). Radiative heat exchange between the dew collector and the cold source is performed by reflection on mirrors (7). The chamber (4) is separated from the cold source (1) by an IR transparent double windows (6). Condensation inside the chamber is observed with optical cameras through two PMMA (plexiglas) windows (8) and (9). Alternatively, window (8) on top of the chamber can be replaced by an IR temperature sensor to monitor the surface temperature of the object (2). Three thermocouples (T1, T2, T3) measure the temperature of incoming air, mirrors

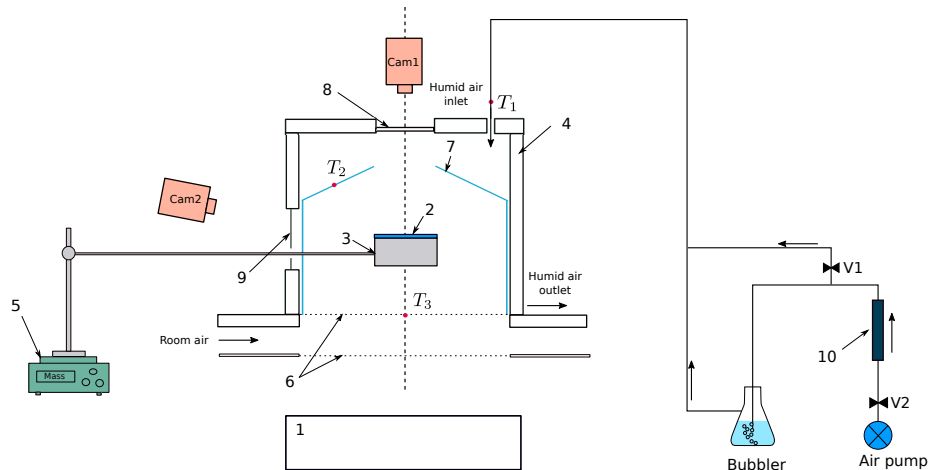


Figure 1: Schematics of the experimental setup (not at scale). 1: Cold source ; 2: Dew collector ; 3: Sample holder ; 4: Cylindrical chamber ; 5: Balance ; 6: IR transparent window ; 7: Mirrors ; 8 and 9: Visualization windows ; 10: Flowmeter ; arrows: Direction of air flow. Interrupted line: Axis of revolution.

and double IR window, respectively,

2.1. Cold source

We use solid carbon dioxide CO_2 ("dry ice") as a cold source (1). Dry ice pellets are cylinders about 1 cm thick and 1 to 5 cm long, stored in a styrofoam box. The temperature of dry ice in equilibrium with its vapour at atmospheric pressure is of 194.7 K, ensuring a constant temperature of the cold source. No liquid carbon dioxide is formed during the sublimation process thereby simplifying its use. The sublimation rate is low but a refill of the vessel every hours is necessary to maintain a stabilized radiative heat flux. When exposed to room humid air, dry ice pellets are covered by a layer of frozen water forming ice crystals, which may modify the surface temperature. Despite of this layer, no significant modification of the radiative cooling power was observed. Ice water emissivity being approximately $\varepsilon_g \approx 0.98$ [20] and the presence of water crystals suggesting a diffuse emission of infrared light, the cold source can thus be considered as a black body. Finally, the density of CO_2 in its

gaseous form at 194.7 K is larger than the air density, making cold CO₂ vapour flowing downward, therefore not disturbing the window (6) situated above the cold source.

2.2. Humidity control

The setup is designed to alternatively work in a "dry air" or in a "humid air" modes. The "dry air" mode actually means that air is at room relative humidity (RH), generally on order 50 % (RH is the ratio of ambient vapour pressure to the saturation pressure at ambient temperature). In this mode, the valve $V1$ is in open position and let ambient air go directly to the chamber (see fig. 1). In the "humid air" mode, the valve $V1$ is closed and the air passes through a bubbler at room temperature, which increases its relative humidity. An adjustable valve $V2$ situated in the flowmeter at the outlet of the pump controls the flow rate. An air flow rate value of $Q = 1.46 \times 10^{-5} \text{ m}^3.\text{s}^{-1}$ is used in all the experiments, corresponding to a mean air flow velocity around the sample holder (3) of $V = Q/(S_0 - S_s) = 3.4 \text{ mm.s}^{-1}$, S_0 being the internal section of the chamber (4) and S_s the section of the sample holder. The RH value inside the chamber cannot be directly measured because of possible IR exchange between the RH sensor and the cold source. Instead we use the fact that no condensation occurs on the mirrors, meaning that their temperature T_2 is larger than the dew point temperature T_d corresponding to a humid air temperature of T_a . From the expression of $T_d(RH, T_a)$ [21] we get the maximum possible value of the relative humidity RH inside the chamber. Typical values of $RH \approx 95 \%$ are obtained with $T_a = 298.3 \text{ K}$ and $T_2 = 297.5 \text{ K}$ (see section 3.2). The fact that RH is close to 100 % is corroborated by the determination of the injected mass of water in air measured by weighing the bubbler during a typical experiment. A high value of relative humidity is used in order to reduce the duration of the experiments. Indeed, as can be seen in Supplementary Informations, experiments performed at a lower humidity ratio (89 %) show a lower condensation rate. Although the dew point temperature T_d is close to the temperature of the air at this humidity level ($T_a - T_d = 0.85 \text{ K}$) it is well

known that dropwise condensation needs supersaturation to form, corresponding to at least several degrees below the dew point temperature (see e.g. [22]). The needed temperature drop is provided to the sample (Fig. 7) through the radiative exchange with the cold source which is the only heat sink of the system. As a matter of fact, no condensation is observed on the mirrors nor on the transparent window, a phenomenon which would have shut down the radiative transfer, whereas thermocouples measure temperature close to T_d as can be seen in Fig. 7. Note that high relative humidity has usually a detrimental effect on radiative cooling, but it does not impact the radiative cooling in our system considering the small size of the device [23, 24]. In the latter references are estimated the transmission decrease in the atmospheric window; for a typical experimental path length of 20 cm (density-length product $m_w = 4.4 \times 10^{-4}$ g.cm⁻², see [25]), it leads to an attenuation of about 4×10^{-4} , i.e. negligible.

2.3. Radiative heat exchanges

The cold source (simulating the nocturnal sky) is situated below the dew collector. In order to perform radiative exchange above the sample, mirrors have been positioned inside the chamber and around the dew collector and its holder. Their role is to connect radiations emitted from the dew collector and the cold source. Figure 2 shows the shape of the mirrors and their dimensions. Mirrors are composed of 1 mm thick Mylar sheet on which is stuck a laminated aluminum sheet on the inside face. The low emissivity of aluminum foil ($\varepsilon_{alu} \approx 0.04$, normal emissivity between 4.5 and 40 μm [26]) makes the mirrors highly reflective to mid-infrared radiations.

The sample holder (3) supporting the dew collector is positioned at the center of the chamber, and thus experiences radiative heat exchanges with the cold source by its lower and side surfaces. For that reason, care must be taken to prevent it from becoming cooler than the dew collector. In that case, an undesirable conductive cooling of the dew collector by the sample holder would take place. A careful design of the sample holder is thus a key step for the control of the radiative exchanges. Figure 2 shows the sample holder and its dimensions.

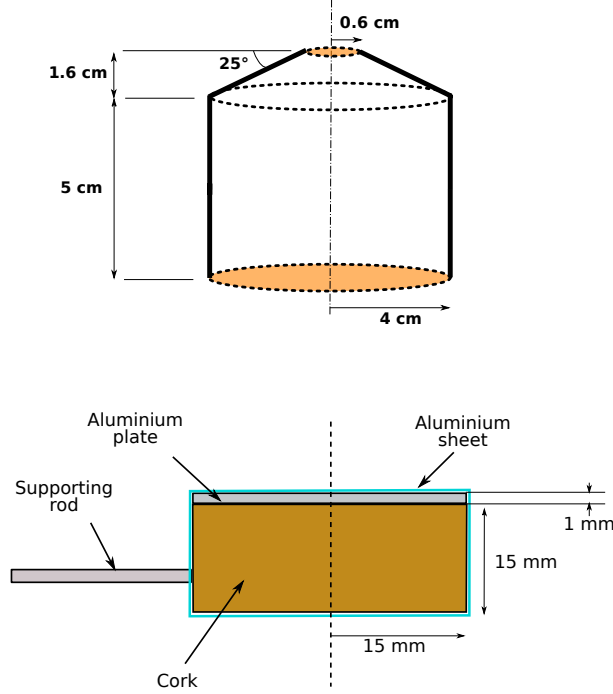


Figure 2: Top : Schematics of the mirrors (7), the colored zones corresponds to the openings to the outside. The interrupted line shows the axis of revolution. Bottom : Schematics of the sample holder (3). The interrupted line shows the axis of revolution.

It is composed of a cylinder of 15 mm height and 15 mm radius made with a thermal insulating material (natural cork). On top of the holder lies a circular plate of aluminum of the same radius and of 1 mm thickness. The cork thermal conductivity measured by the hot plate method [27] is $\lambda_c = 0.057 \text{ W.m}^{-1}.\text{K}^{-1}$. The aluminum plate insures a perfectly plane top surface with a large thermal conductivity ($\lambda_a \approx 240 \text{ W.m}^{-1}.\text{K}^{-1}$) [28]. An additional thermal resistance between the aluminum plate and the cork participates in the insulation of the top face. Finally, the cork cylinder and the aluminum plate are folded together into an aluminum sheet of low emissivity, in order to minimize the radiative exchanges between the bottom surface of the sample holder and the cold source.

In order to validate the design of the radiative chamber, we have performed a modelling of thermal exchanges between the dew collector (2) and the rest of

the chamber. The aim of the modelling is to calculate the incoming radiative heat flux on dew collector (2) and on sample holder (3), and to study the influence of radiative properties of these surfaces. The model is based on some hypothesis : i) The double window is a single transmittive interface ; ii) IR emissions are isotropic ; iii) Reflections are diffusive ; iv) Surfaces are homogeneous and isothermal grey bodies (except surface 3 whose transmittive properties are wavelength dependent) and v) Air is a totally transparent media. We recall that in a N faces enclosure, for isotropic emissions and diffuse reflections, the radiosity of face i is the radiative heat flux leaving face i and composed of the radiation emitted by the surface itself and the radiation coming from other faces and reflected by face i . Radiosity J_i of face i is thus expressed as

$$J_i = \varphi_i^e + \rho_i \sum_{j=1}^N F_{ij} J_j \quad (1)$$

with ρ_i the reflection coefficient of surface i and F_{ij} the view factor between i and j , that is the fraction of heat flux emitted by j and intercepted by i . φ_i^e is the heat flux density emitted and/or transmitted by surface i .

Solving equation 1 for all surfaces of the enclosure (see Appendix A for details) then lead to the expression of the incoming heat flux density as

$$\varphi_i^i = \sum_{j=1}^N F_{ij} J_j \quad (2)$$

Of particular interest are the following expressions for the incoming heat flux density on the different faces (5 : bottom), (7 : top) and (11 : side) of the sample holder (see Appendix A. for schematic).

Table 1 shows the resulting numerical values of the incoming heat flux for the lower (5), upper (7) and lateral (11) faces of the sample holder for three different configurations. Case 1 ($\varepsilon_5 = 0.04$, $\varepsilon_7 = 0.95$, $\varepsilon_{11} = 0.04$) corresponds to a highly emissive sample collector. Case 2 ($\varepsilon_5 = 0.04$, $\varepsilon_7 = 0.04$, $\varepsilon_{11} = 0.04$) corresponds to a low emissive sample collector. Case 3 ($\varepsilon_5 = 0.04$, $\varepsilon_7 = 0.95$, $\varepsilon_{11} = 0.95$) corresponds to the upper and side faces of the sample holder wetted by condensed water, their emissivity being modified by the presence of drops.

	φ_5^i (W.m ⁻²)	φ_7^i (W.m ⁻²)	φ_{11}^i (W.m ⁻²)
Case 1 ($\varepsilon_5=0.04$, $\varepsilon_7=0.95$, $\varepsilon_{11}=0.04$)	316.4	365.1	347.2
Case 2 ($\varepsilon_5=0.04$, $\varepsilon_7=0.04$, $\varepsilon_{11}=0.04$)	314.9	350.8	339.1
Case 3 ($\varepsilon_5=0.04$, $\varepsilon_7=0.95$, $\varepsilon_{11}=0.95$)	319.2	377.3	362.0

Table 1: Incoming radiative flux densities on the three faces of the sample holder : (5) Lower face ; (7) Upper face ; (11) lateral face, for different values of the faces emissivities.

From the knowledge of the incoming heat flux densities the distribution of temperature in the bulk of the sample holder (3) is simulated to confirm that the conductive flux is directed towards its upper surface (2), i.e that this later surface is not conductively cooled. For that we solve the stationary energy equation $\Delta T = 0$ in 2D axisymmetric coordinates as shown in Figure 3 :

$$\frac{1}{r} \frac{\partial}{\partial r} \left(r \frac{\partial T}{\partial r} \right) + \frac{\partial^2 T}{\partial z^2} = 0 \quad (3)$$

with following boundary conditions on the three faces (5), (7) and (11) :

$$-\lambda_l \nabla T = h_i (T - T_a) - \varepsilon_i \varphi_i^i + \varepsilon_i \sigma T^4 \quad (4)$$

with λ_l the bulk material thermal conductivity, σ the Stefan-Boltzmann constant, T the local temperature, T_a the air temperature and φ_i^i the incident radiative heat flux density incoming on surface i of emissivity ε_i . The convection coefficient h_i applied to surface i is calculated from natural convection correlations : $h_5 \simeq 4.4$ W.m⁻².K⁻¹ [29], $h_7 \simeq 4.8$ W.m⁻².K⁻¹ [30] and $h_{11} \simeq 6.3$ W.m⁻².K⁻¹ [31]. Note that expression (4) is only valid in the "dry" mode. In order to take into account the latent heat of condensation, the term $a_w L(p_v(T_a) - p_s(T))$ has to be added to Eq. 4, with a_w the water vapor transfer coefficient, L the latent heat of condensation of water, $p_v(T_a)$ the partial pressure of water vapor at temperature T_a and $p_s(T)$ the saturation pressure of

water vapor at temperature T [2]. Figure 3 shows the results of the simulation with and without condensation, for air temperature $T_a = 298.3$ K (see section 3) and with emissivity of the upper support surface varying from 0.04 to 1.

From table 1 and figure 3 it can be seen that 1) condensation on the sample holder can slightly modify the incoming radiative heat flux and that 2) heat is transferred from the lower face of the sample holder to its upper face, indicating that the cooling of the upper face is only due to radiative exchanges.

2.4. IR transparent double-window

To separate the humid air from the cold source, an IR transparent double-window (6) in Fig.1 is used to close the chamber while permitting a radiative heat transfer with the cold source. The double-window is composed of two parallel polypropylene films of $15\text{ }\mu\text{m}$ thickness and 8 cm diameter, and separated from each other by 13 mm. The upper film closes the chamber. The films are not perfectly transparent to infrared radiations and are also radiatively cooled by the cold source, which can lead to some condensation on the upper film inside the chamber. Water being opaque to IR light, it decreases the transmission coefficient of the film and hinders radiative exchange. To avoid such a condensation, a second film is placed below the first film and an air stream (from the room) is blown in the gap between films to warm up the upper film.

The radiative properties of the polypropylene films are measured in the wavelength range $[2.5 - 25]\text{ }\mu\text{m}$ by infrared spectroscopy in the direction normal to the film. The radiative properties of the double window composed of the two films are calculated from the properties of each single film and the analysis of the reflections between the two films [32]. Figure 4 shows the spectral transmission coefficient of single and double films. Considering an incident flux corresponding to a black body at $T \simeq 195$ K (i.e. the temperature of the cold source), the integration of the transmission coefficient in the range $[2.5 - 25]\text{ }\mu\text{m}$ gives $\tau = 0.92$ for a single film and $\tau = 0.86$ for the double-window.

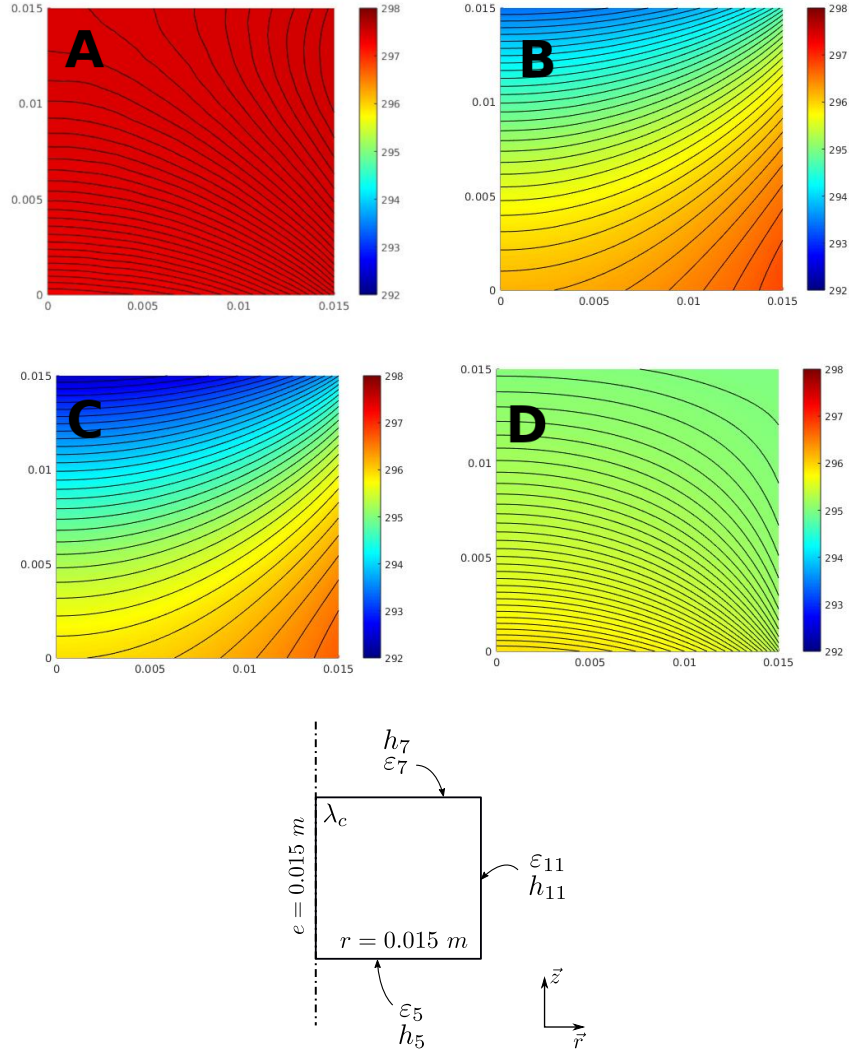


Figure 3: Numerical simulation of temperature distribution inside the support. Temperature scale is in K. A: Case 2, $\varepsilon_5 = 0.04$, $\varepsilon_7 = 0.04$, $\varepsilon_{11} = 0.04$; B: Same as case 1 but with sample of lower emissivity, $\varepsilon_5 = 0.04$, $\varepsilon_7 = 0.7$, $\varepsilon_{11} = 0.04$; C: Same as case 1 but with sample of higher emissivity, $\varepsilon_5 = 0.04$, $\varepsilon_7 = 1$, $\varepsilon_{11} = 0.04$; D: Case 3, $\varepsilon_5 = 0.04$, $\varepsilon_7 = 0.95$, $\varepsilon_{11} = 0.95$ (condensation). $T_a = 298.3$ K. Side view of the sample support. h_j : Convection coefficient applied to face j ; φ_j^i : Incident radiative heat flux density to face j ; φ_j^e : Radiative heat flux density emitted by the surface j . λ_c : Cork conductivity.

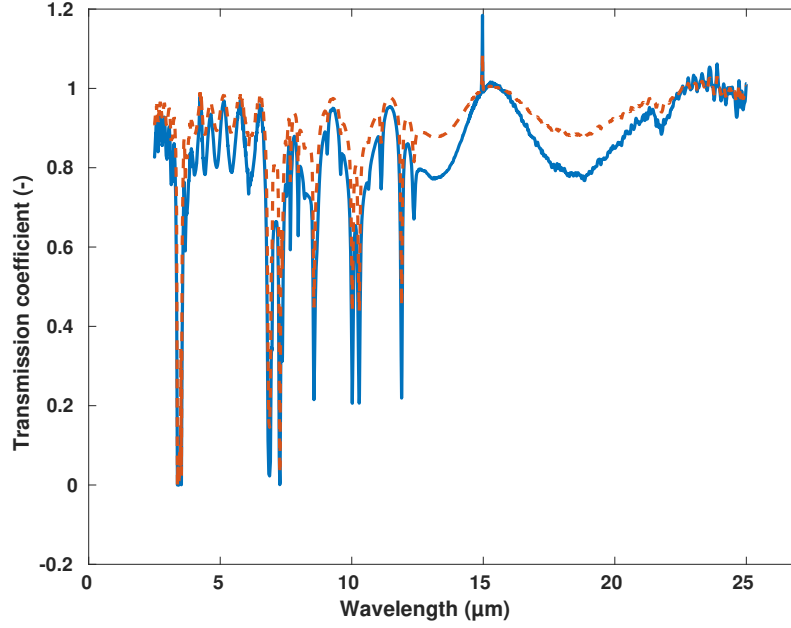


Figure 4: Spectral transmission coefficient of a single sheet of polypropylene measured by IR spectroscopy (dashed line) and of two superimposed sheets of polypropylene calculated by the reflection method (plain line).

2.5. Measurements

Visualization of the condensation process is performed by two cameras (DFK 23U445 from TheImagingSource), at 30 fps and with a 1280×960 px CCD sensor. With camera Cam1, the condensation rate on the upper surface of the sample is determined by a visual method described in [33]. The method is based on the recognition of the contour of each individual droplets, giving access to their radius. Knowing the droplets contact angle on the surface, the volume of each droplet is calculated, and hence the total volume of condensed water on the surface is obtained as a function of time.

The sample holder is resting, with the help of an arm, on a balance (5) positioned outside the chamber. The balance (Sartorius ENTRIS, interfaced with MATLAB) thus measures the total mass of water condensed on the sample

holder with a precision of ± 1 mg and 1 measurement per second. Note that condensation occurs not only on the sample surface (2), but also on the lateral surface of the sample holder.

An IR thermometer can be introduced inside the chamber replacing window (8) by a supporting device. The IR thermometer is a Omega OS-Mini 802 sensor with variable emissivity. It has a precision of ± 1 K, a repeatability of ± 0.5 K and works in the range $[8-14]$ μm . Thermocouples are located at the entrance of the chamber (T1), on mirrors (T2) and on the IR transparent window (T3). They are K-type with a precision of 20 mK and are connected to an acquisition device giving one measurement per second. The use of thermocouples to measure air temperature has to be avoided because the thermocouple can be affected by radiative exchanges. Air temperature inside the chamber is calculated as the mean between inlet air temperature (T1) and mirrors temperature (T2) as $T_{air} = (T1 + T2)/2$, giving typically $T1 - T2 \approx 2$ K.

The incoming radiative heat flux density on the upper surface of dew collector (2) is measured using a sensor (Captec) giving a voltage U_s as a function of the net radiative heat flux density exchanged between the sensor and the environment. Its sensitivity is $K = 0.517 \mu\text{V.W}^{-1}.\text{m}^{-2}$. An integrated thermocouple gives the temperature of the sensor, T_s . Knowing U_s , K and T_s , and considering the sensor as a black body (constructor specification), the value of the incident radiative heat flux density is obtained from

$$\varphi^i = \frac{U_s}{K} + \sigma T_s^4 \quad (5)$$

where σ is the Stefan-Boltzmann constant.

Experimental procedure. To ensure the reproductibility of the results, it is important to go through the following steps. The room thermal stability has to be close to ± 0.1 K. When the room temperature and relative humidity are stabilized, dry ice is inserted in the device, and air stream is sent between the two polypropylene films. The air pump is switched on in "dry air" mode and

the flow rate is adjusted to the value $1.46 \times 10^{-5} \text{ m}^3.\text{s}^{-1}$ with valve V2. The sample surface and sample holder, cleaned with ethanol before use, are inserted in the chamber. Once the thermal equilibrium is reached, the dry ice reservoir is refilled every hour to compensate the volume reduction due to sublimation. Data collection begins at the time $t = 0 \text{ s}$ defined when switching the air circuit to "humid air" mode. It is necessary to readjust the flow rate with V2 as it slightly decreases when passing through the bubbler. Experiment usually ends after $\approx 10000 \text{ s}$ but can be extended if needed.

3. Experimental results

3.1. Radiative versus conductive cooling

This section presents a qualitative experiment which demonstrates the ability of the radiative cooling chamber to achieve water condensation on objects of high thermal resistance. We use as dew collector (2) a small block of PMMA of $10 \times 13 \times 8 \text{ mm}^3$ with thermal conductivity $\lambda_{pmma} = 0.19 \text{ W.m}^{-1}.\text{K}^{-1}$ [28] and mid-IR emissivity $\varepsilon_{pmma} > 0.95$ [34]. The block of PMMA is stuck with thermal grease on the sample holder (3) to insure thermal contact. The temperature of the inlet air is $T_1 = 295 \text{ K}$ and its relative humidity $RH = 95 \%$.

In a first experiment, the cold source (1) of the device is used to radiatively cool the piece of PMMA. Figure 5a shows the distribution of condensed droplets on PMMA surface. Droplets are uniformly distributed all over the surface, excepted at the base where no condensation occurs, and at the vertical and upper edges where droplets grow faster than in the middle. Note that one has to be careful when relating the size distribution of the droplets to the temperature field, as a complex interplay with edge effects occurs. Edge effect are present at the periphery (resp. at the base) of the block where the drops capture more (resp. less) moisture than in the middle of the surface [35]. However, in the center of the block, far from the edges, one can determine isolines of drops of the same size, as represented by white lines in figure 5a. The stationary 3D heat equation was solved in the block to obtain a qualitative appreciation of the

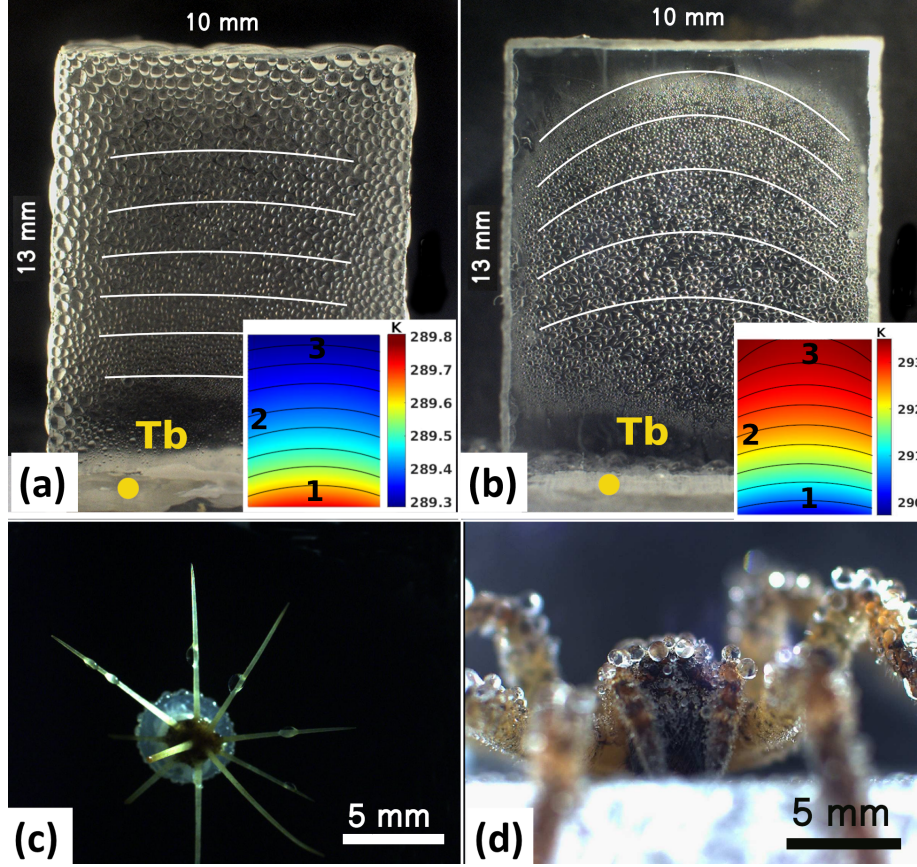


Figure 5: Top : PMMA block ($10 \times 13 \times 8 \text{ mm}^3$) cooled by radiation (a) and conduction (b) from its base (temperature T_b), $t=5830 \text{ s}$ after the beginning of condensation with chamber conditions : $T_1 = 295 \text{ K}$, $\text{RH}=95 \%$, $T_b = 289.8 \text{ K}$. Bottom : condensation obtained by radiative cooling on cactus spines (c) and a spider (d). Inserts in a) and b) : simulated temperature distribution (see text for simulation details)

temperature distribution of its front face, as shown in the insert of figure 5a. Equation 4 was used as boundary conditions for the top face of the block (face 3 in the insert : $\lambda_l = \lambda_{\text{pmma}}$, $h_3 = 5.9 \text{ W.m}^{-2}.\text{K}^{-1}$, $\varepsilon_i = \varepsilon_{\text{pmma}}$, $\varphi^i = 355 \text{ W.m}^{-2}$) and for the vertical faces of the block (face 2 in the insert : $\lambda_l = \lambda_{\text{pmma}}$, $h_2 = 6.4 \text{ W.m}^{-2}.\text{K}^{-1}$, $\varepsilon_i = \varepsilon_{\text{pmma}}$, $\varphi^i = 355 \text{ W.m}^{-2}$). The value of φ^i is calculated from equation A.3b. A positive conductive heat flux of 15 W.m^{-2} was used as boundary condition for the bottom face of the block (face 1 in the insert), in order to

get the temperature $T_b=289.8$ K. From the comparison of isolines in drop size and in temperature we see that there is a gradient in drop size in the center of the block which has the same shape and direction than the simulated thermal gradient. We can infer from these observations that the surface, when cooled by radiation deficit, exhibits higher condensation yield towards the top of the block (and near boundaries thanks to the addition of edge effects).

In a second experiment, the cold source (1) is removed and the bottom face of the sample holder (3) is in contact with a Peltier cooling stage, whose temperature is homogenized by a thick electrolytic copper plate (env. 5 mm). The power of the Peltier is adjusted such as the temperature of the top face of the holder surface is the same as in the first experiment, *i.e.* $T_b = 289.8$ K. Figure 5b shows that the distribution of condensed drops on the PMMA surface is very different from the first experiment. In this case of conductive cooling, the thermal conditions necessary to condensation are met only in the middle part of the PMMA surface, where droplets are larger than droplets situated at the edges of the block. Indeed, condensation at the base is prevented in the same way as with radiative cooling. However, no condensation occurs at the upper edge of the block and on lateral edges. As well as for the first experiment, the heat equation were solved inside the PMMA block. The result is plotted in the insert of figure 5b. A conductive heat flux of -110 W.m^{-2} were used as boundary condition of the bottom face of the block (face 1 in the insert), consequently with a base temperature of $T_b=289.8$ K. A convective heat flux with coefficient of respectively $h_3=5.9 \text{ W.m}^{-2}.\text{K}^{-1}$ and $h_2=6.4 \text{ W.m}^{-2}.\text{K}^{-1}$ were used for the boundary conditions of the horizontal top face 3 resp. vertical faces 2 of the block. The comparison of the isolines confirms that the block is cooled by conduction. Moreover it shows that a thermal gradient is created from the base to the top of the PMMA block such as its upper edge, acting as a thermal fin, is heated by air convection and is not sufficiently cold to insure droplet condensation. Note that the isotherm corresponding to the condensation limit does not equal the dew point temperature of $T_d = 294.2$ K, consequently with the supersaturation associated with heterogeneous nucleation.

To further illustrate the potentialities of the device for cooling complex 3D surfaces, Figures 5c and 5d show that condensation successfully proceeds on dew collectors (2) of complicated 3D shapes, such as a cactus spine and a spider. For these structures, cooling by thermal contact is inefficient. As an example, a simplified calculation of the temperature distribution in an infinite circular thermal fin of radius $r_f = 100 \mu\text{m}$ with thermal conductivity $\lambda_f \approx 0.2 \text{ W.m}^{-1}.\text{K}^{-1}$ (wood conductivity [36]) can be made. With a base temperature $T_0 = 22^\circ\text{C}$ in a surrounding air at $T_a = 25.1^\circ\text{C}$ (temperatures for a classical experiment, see sec. 3.2.2), the convection coefficient for free convection around the fin is estimated to be $h_f \approx 500 \text{ W.m}^{-2}.\text{K}^{-1}$ [37]. The temperature distribution $T = f(x)$ along the fin can be expressed as $\theta(x)/\theta_0 = \exp(-mx)$ with $\theta(x) = T(x) - T_a$, $\theta_0 = T_0 - T_a$ and $m^2 = 2h_f/\lambda_f r_f$ [38]. Condensation conditions are met in the fin while $T(x) < T_d$, or $x < x_d$. Solving the previous equation then lead to $x_d \approx 0.15 \text{ mm}$. This calculation shows that thermal conditions needed for condensation wouldn't be met in the cactus spine if just cooled by conduction. Further investigations on the thermal aspects of radiative condensation on cactus spines would nevertheless be interesting. Finally for the spider example, the fact that bigger drops are situated on top of it suggests, as well as figure 5.a, that a thermal gradient is present from the top to the bottom of the spider, inconsistent with conductive cooling.

3.2. Radiative cooling of model surfaces

This section presents quantitative results for radiative condensation obtained on planar model surfaces. The condensation surface (2) is a circular thin sheet of 30 mm diameter made of a composite material specially designed to control the emissivity and contact angle with water. Three composites of different emissivity and water contact angle were designed. Composite 1 (C1) is composed of a foil of laminated aluminum, and two foils of poly-vinyl chloride (PVC) of 250 μm and 140 μm thickness on top of it, leading to an overall emissivity $\varepsilon_{C1} = 0.96$, and a contact angle with water $\theta_{C1} = 84.6^\circ \pm 3.6^\circ$. Composite 2 (C2) is composed of a foil of laminated aluminum, a foil of PVC of 250 μm thickness

and a foil of Polyethylene of 6 μm thickness on top of it, leading to an emissivity $\varepsilon_{C2} = 0.88$. Composite 3 (C3) is composed of a foil of laminated aluminum, and a foil of Polyethylene (PE) of 6 μm thickness on top of it, leading to an emissivity $\varepsilon_{C3} = 0.05$. The contact angle with water of C2 and C3 is the same, $\theta_{C2} = \theta_{C3} = 65.9^\circ \pm 3.6^\circ$. The values of the emissivity have been obtained from the comparison between the luminance of the composite, measured by an IR camera (FLIR), and the luminance of a material of known emissivity (PVC, $\varepsilon = 0.96$) at the same temperature. The measured emissivities are total emissivities integrated over the spectral range $[7.5 - 14] \mu\text{m}$, corresponding to the range of the IR camera, and in the direction normal to the surface.

During the condensation experiment, room air is maintained at temperature $T_{ext} = 299.2 \text{ K}$ and relative humidity $RH = 45 \%$. Figure 6 shows that the temperature of incoming air, mirrors and IR transparent double-window are stable during the experiments, except for small oscillations due to the control of ambient room temperature. Under these conditions, air inside the chamber is at the temperature $T_{air} = (T_1 + T_2)/2 = 298.3 \text{ K}$ and relative humidity $RH = 95 \%$.

3.2.1. Radiative deficit

The incident radiative heat flux density onto the composite surface C1 is measured with a flux sensor placed on the composite surface C1, measuring a voltage that is converted into a heat flux through Eq.5. Figure 7 shows the values of temperatures measured by thermocouples T_1 , T_2 and T_3 as well as the temperature of the flux sensor T_s , just after the latter is inserted into the device. The evolution of the measured voltage U_s is also plotted.

In the steady state without condensation, this flux has value $\varphi_{C1}^i = 368.3 \pm 0.3 \text{ W.m}^{-2}$. It is interesting to note that this experimental value compares well with the corresponding value obtained by the numerical modelling of the thermal exchanges (see φ_7^i in case 1 of table 1), as well as the temperature of the sensor positioned on the top surface (7) of the sample holder which corroborates the temperature found by numerical simulation (see figure 3). These measurements

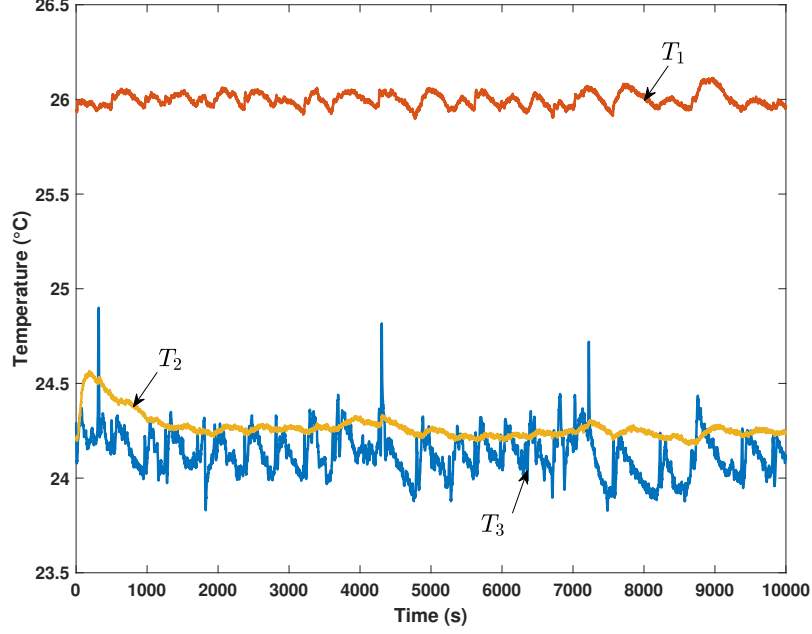


Figure 6: Temperature evolution of incoming air (T_1), mirrors (T_2), and IR transparent window (T_3) during a condensation experiment. See Figure 1 for location of the thermocouples.

thus validate the fact that the cooling of the upper surface of the sample holder, and by extension the sample itself, is only radiative.

The radiative deficit applied to the surface of the C1 composite can be written as

$$\varphi_{rad} = \varepsilon_{C1}\varphi_{C1}^i - \varepsilon_{C1}\sigma(T_c^0)^4 \quad (6)$$

T_c^0 is the temperature of the C1 surface in steady state without condensation (for $t < 0$ s in the experiment). With $T_c^0 = 22$ °C (from figure 8) and $\varepsilon_{C1} = 0.96$, one get $\varphi_{rad} = -59.5$ W.m⁻². This radiative deficit is close to the natural radiative deficit from atmosphere under conditions of dew formation, which ranges from ~ 60 W.m⁻² to 100 W.m⁻² [2, 39]. It is also comparable to the cooling power of other dew chambers where values of -71.9 W.m⁻² [10] and -67.7 W.m⁻² [14] have been reported.

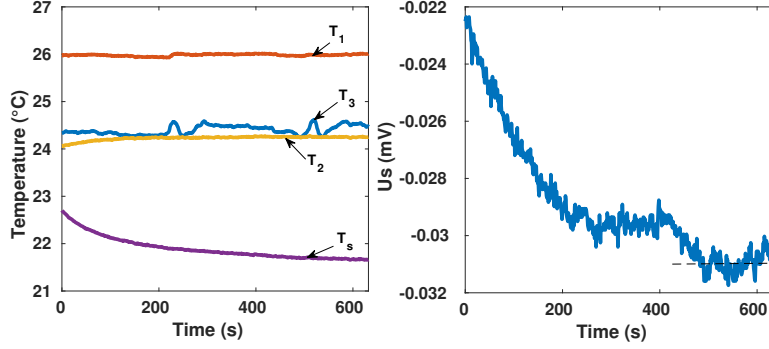


Figure 7: Temperatures of T_1 : incoming air, T_2 : mirrors, T_3 :IR transparent window and T_s : sensor, during a radiative heat flux measurement. U_s : voltage measured by the radiative heat flux sensor.

3.2.2. Condensation rate

Figure 8 presents data collected during a condensation experiment using the composite C1 as dew collector (2).

Curve A depicts the temperature T_s of an IR thermocouple sensor focused on the C1 surface, showing two regimes. A first regime occurs between t_0 and t_c , where the temperature of the sensor increases rapidly from $T_c^0 = 22$ °C at the beginning of the experiment, without condensation, and a second regime after time t_c where temperature progressively decreases until a constant value $T_c^\infty = 22.4$ °C, indicating the steady state of condensation. Curve B depicts the evolution of the water-condensed mass on the C1 surface, as measured by the visual method (see section 2.5 and [33]). Figure 9 shows the growth dynamics of droplets on the C1 surface. The evolution is linear, with a steady condensation rate $\dot{m} = 1.0 \times 10^{-5}$ g.s⁻¹.

The evolution of mass as indicated by the balance during the experiment is depicted in Figure 8 as Curve C. The evolution of weighed mass is concerned with the total mass condensed on the whole surface exposed to condensation, i.e. not only the C1 surface but also the lateral and bottom surfaces of the sample holder (3). The weighed mass increases non-linearly until time $t_d \approx 2500$ s, after which the condensation rate reaches a steady state, yielding a constant rate

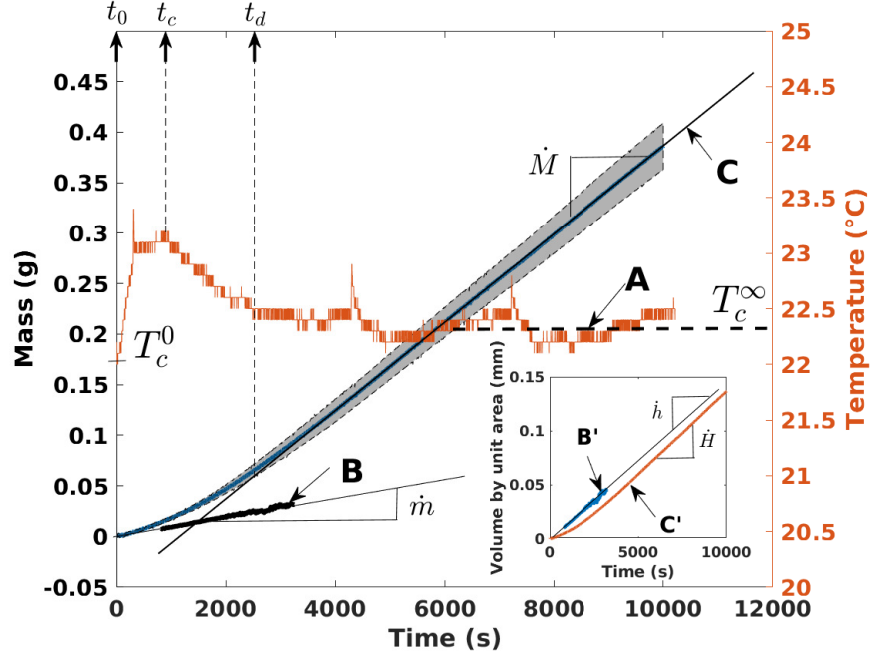


Figure 8: Experiments with Composite 1 (C1) with $T_a = 25.1$ °C (298.3 K) and $RH = 95$ %. Curve A: Temperature T_S of an IR thermocouple sensor focused on the C1 surface : $T_c^0 = 22$ °C at the beginning of the experiment, without condensation, $T_c^\infty = 22.4$ °C in steady state of condensation. Curve B: Mass of droplets condensed on the C1 surface with a condensation rate $\dot{m} = 1 \times 10^{-5}$ g.s $^{-1}$, measured with the visualization method. Curve C : Mass of droplets condensed on the surface {C1 + lateral surface+ bottom surface} with a condensation rate $\dot{M} = 4.55 \times 10^{-5}$ g.s $^{-1}$, measured with the balance. The grey zone around C represents the uncertainty due to the presence of the camera or IR thermocouple (see text). Curves B' and C' : same as B and C but the condensed mass has been converted in volume per unit surface, yielding $\dot{h} = 1.4 \times 10^{-5}$ mm.s $^{-1}$ (C1) and $\dot{H} = 1.6 \times 10^{-5}$ mm.s $^{-1}$ (C1 + lateral and bottom surface). t_0, t_c, t_d : times related to condensation regimes (see text).

$\dot{M} = 4.55 \times 10^{-5}$ g.s $^{-1}$. The non-linear evolution observed at the beginning of curve C can be attributed to a transient regime due to 1) the establishment of a new energy balance initiated by the release of latent heat L from condensation as $\phi_{lat} = Ldm/dt$ with dm/dt the mass condensation rate and ϕ_{lat} the latent heat flux ; 2) the modification of the surface emissivity, and by extension of the radiative deficit (see eq. 6), due to droplet condensation as discussed below ;

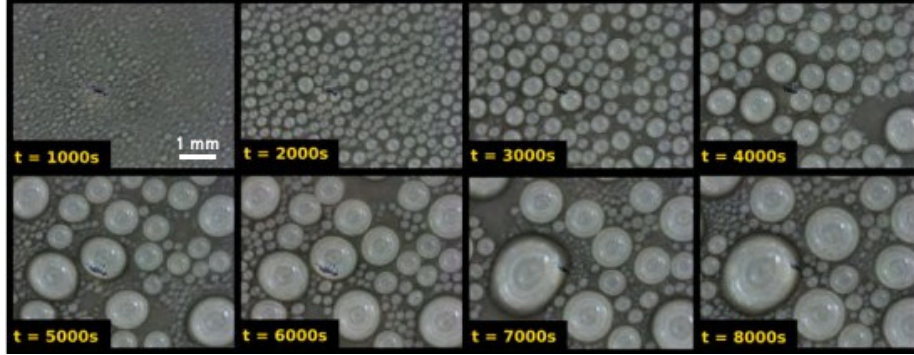


Figure 9: Visualization of the evolution of condensation obtained by radiative cooling on the surface C1 with $T_a = 298.3$ K and $RH = 95$ %. Size of the pictures : 6.1×4.6 mm².

3) the delayed condensation on the lateral surface of (3), due to its lower emissivity and hence higher temperature, as compared to the C1 surface. Note that the IR measurement of the surface temperature and the droplets visualization cannot be simultaneously performed, thus two condensation experiments had to be carried out to obtain figure 8, the reproductibility being ensured by the monitoring of temperatures in the radiative chamber and in the room. However, a slight difference in the weighed mass is observed, due to the presence of the camera or the IR thermocouple, which have a small but noticeable impact on the thermal conditions of the device. The mean of the two experiments is thus plotted with the associated uncertainty as represented by the grey zone.

The insert in Figure 8 presents the evolution of the condensed-water volume per unit surface (in mm or L.m⁻²) as obtained by dividing the condensed mass by the density of water ($\cong 1000$ kg.m⁻³ at 295.6 K) and by the area of the surface exposed to condensation. The data of curve B are concerned with the C1 top surface of sample holder (3), of area 707 mm². We thus obtain curve B' with a constant rate $\dot{h} = 1.4 \times 10^{-5}$ mm.s⁻¹. For the data of curve C, the condensation occurs on top, bottom and lateral surfaces of the sample holder (3), corresponding to a total area of 4×707 mm². We thus obtain curve C', which is situated below curve B' at any given time. After 2500 s, curve C' becomes almost parallel to curve B', with a steady condensation rate characterized by

a constant slope $\dot{H} = 1.6 \times 10^{-5} \text{ mm.s}^{-1}$, close to \dot{h} . Note that during a 10 hours experiment, a total condensed-water volume of $v \cong 0.5 \text{ L.m}^{-2}$ would be obtained. As a comparison outdoor dew yield (for one night) is reported to range from 0.12 L.m^{-2} [40] in Ajaccio (France) to 0.6 L.m^{-2} [7] in Kothara (India). Our experiment thus produces an amount of dew comparable to natural dew condensation. To our knowledge the only quantitative study in terms of condensation rate in indoor experiments were performed by Went in 1978 [14] on watermelon leaves. Went found an artificial dew yield of about $2.6 \times 10^{-6} \text{ mm.s}^{-1}$, corresponding to 0.11 L.m^{-2} for a 12h night duration.

When comparing the curves B' and C', it has to be stressed that despite the fact that they are concerned with surfaces of different emissivities, the condensation rate obtained in steady state is nearly the same. This suggests that the emissivity of the surface has a strong influence on the onset of condensation and on the transient regime, but its influence reduces as more and more water droplets of high emissivity cover the surface.

The effect of the surface emissivity on the condensation rate can be further studied using composites C1, C2 and C3 as dew collector (2). C2 and C3 surfaces have the same contact angle with water, but quite different emissivities (0.88 and 0.05 respectively). The evolution of the mass of water weighed by the balance during a condensation experiment is shown in Figure 10.

The evolution curves exhibit a transient non-linear evolution followed by a linear evolution. The transient regime is longer for the low emissivity C3 surface (lag time of $t_3^0 \cong 2200 \text{ s}$) than for the high emissivity C1 and C2 surfaces ($t_1^0 \cong 1100 \text{ s}$ and $t_2^0 \cong 1600 \text{ s}$). In the linear (steady state) regime, the curves are nearly parallel, with similar rates of condensation $\dot{M}_1 = 4.55 \times 10^{-5} \text{ g.s}^{-1}$, $\dot{M}_2 = 3.95 \times 10^{-5} \text{ g.s}^{-1}$ and $\dot{M}_3 = 4.13 \times 10^{-5} \text{ g.s}^{-1}$, respectively. A first conclusion to be drawn from these experiments is that the difference in emissivity leads to a significant difference in accumulated dew yield at a given time (see Figure 10). A second conclusion is that the limiting effect of a low emissivity of the surface disappears progressively as condensation proceeds and water droplets of high emissivity ($\cong 0.95$ [41]) are covering the surface. For high values of substrate

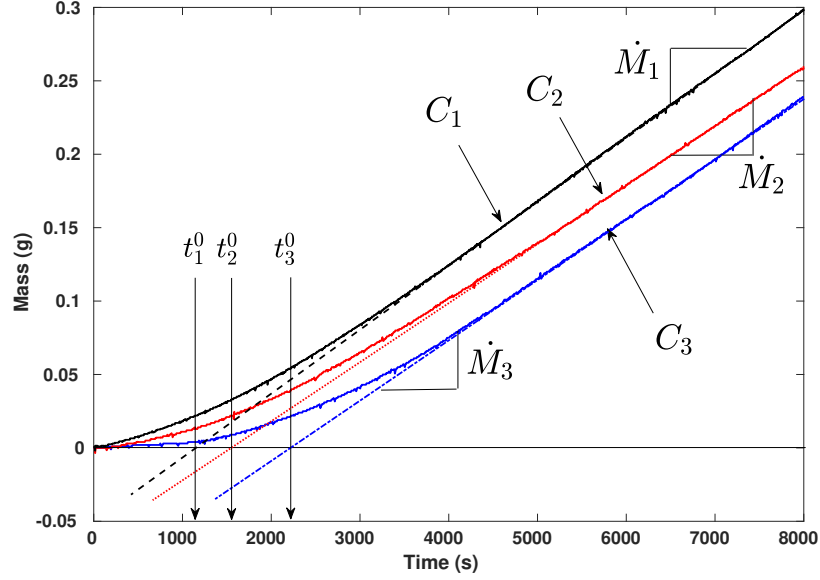


Figure 10: Evolution of the mass weighed by the balance during the condensation obtained by radiative cooling of surfaces (2) of different emissivities and contact angle : Surface C1 ($\varepsilon_{C1} = 0.96$, $\theta_{C1} = 84.6^\circ$), Surface C2 ($\varepsilon_{C2} = 0.88$, $\theta_{C2} = 65.9^\circ$), Surface C3 ($\varepsilon_{C3} = 0.05$, $\theta_{C3} = 65.9^\circ$). Chamber conditions are $T_a = 298.3$ K and $RH = 95\%$.

emissivity the condensation rate seems to be independent of the contact angle of water on the substrate. Further experiments need to be performed on low emissive substrates in order to probe the influence of the contact angle, which determines the surface coverage of water [42] and thus the effective emissivity of a condensing surface.

4. Conclusion

We have shown that quantitative data of water condensation (dew) can be obtained in the laboratory by radiative cooling of surfaces. The device developed in this study provides radiative deficit and condensation rates comparable to those observed for natural (outdoor) dew. The device is thus applicable to the quantitative study of dew itself and its effects on plants and small animals,

as well as dew atmospheric chemistry, and more generally of any natural radiative cooling applications. Of particular interest is its ability to radiatively cool surfaces of various complicated shapes, for which contact cooling is inefficient. Moreover, systematic studies concerning surfaces with different radiative and wetting properties can be carried out, helping to design optimal surfaces before field tests. The limitations of the device are, firstly, its relatively small size, which can nevertheless be easily improved by rescaling the setup. Secondly, the weighing system, which is inherently exposed to the cold source radiations, also collects dew water during experiment and imposes comparative studies. Finally, the angular distribution of the incoming radiation on the sample is different from the atmosphere distribution. A larger device could be useful to control the angular distribution. Also, further experiments with a fine control of humidity would allow to explicitly link the condensation rate and the supersaturation inside the device. The results obtained with surfaces of contrasted emissivities raise an interesting question, that is to quantify the evolution of the effective emissivity of a surface during condensation, with water droplets of high emissivity progressively covering the underlying surface.

Appendix A. Radiative heat flux

In order to validate the design of the radiative chamber, we have performed a modelling of thermal exchanges between the dew collector (2) and the rest of the chamber. The aim of the modelling is to calculate the incoming radiative heat flux on dew collector (2) and on sample holder (3), and to study the influence of radiative properties of these surfaces. The difficulty comes from the fact that the radiation emitted by the surfaces is reflected by the mirrors.

The different surfaces involved in the radiative heat transfer are depicted in Figure A.11 and their properties are listed in Table A.2. Hypothesis of the model are detailed in section 2.3.

Radiosity J_i of face i is expressed by equation 1 where φ_i^e is the heat flux

Surface	Name	Material	Radiative properties
1	Cold source	Black body	$\varepsilon_1 = 1$
2	External environment	Black body	$\varepsilon_2 = 1$
3	Double window	Polypropylene Film	$\tau \simeq 0.86$
4	Mirrors	Aluminum	$\varepsilon_4 = 0.04$
5	Lower support face	Aluminum	$\varepsilon_5 = 0.04$
6	Virtual boundary	-	$\varepsilon_6 = 0 ; \tau_6 = 1$
7	Upper support face	variable	$0.04 \leq \varepsilon_7 \leq 0.96$
8	Mirrors	Aluminum	$\varepsilon_8 = 0.04$
9	External environment	Black body	$\varepsilon_9 = 1$
10	Mirrors	Aluminum	$\varepsilon_{10} = 0.04$
11	Side support face	Aluminum	$0.04 \leq \varepsilon_{11} \leq 0.95$
12	Mirrors	Aluminum	$\varepsilon_{12} = 0.04$
13	Virtual boundary	-	$\varepsilon_{13} = 0 ; \tau_{13} = 1$

Table A.2: Surfaces, materials and radiative properties ; ε : Global hemispherical emissivity ; τ : Transmission coefficient ; "-" indicates that the property is not defined.

heat flux density φ_i^i on surface i is calculated as

$$\varphi_i^i = \sum_{j=1}^N F_{ij} J_j \quad (\text{A.2})$$

Finally, a system of N equations is obtained which is solved knowing the radiative properties and temperatures of each surface. Of particular interest are the following expressions for the incoming heat flux density on the different faces (5),(7) and (11) of the sample holder :

$$\varphi_5^i = F_{53} J_3 + F_{54} J_4 \quad (\text{A.3a})$$

$$\varphi_7^i = F_{78} J_8 + F_{79} J_9 + F_{710} J_{10} \quad (\text{A.3b})$$

$$\varphi_{11}^i = F_{116} J_{6s} + F_{1113} J_{13i} + F_{1112} J_{12} \quad (\text{A.3c})$$

Values of incoming heat flux densities on these surfaces are summarized in

table 1 for different sets of emissivities.

Acknowledgements

We thank the Institut de Minéralogie, de Physique des Matériaux et de Cosmochimie de Sorbonne Université (UMR 7590-Sorbonne Université-CNRS-MNHN/IRD) for the spectroscopy measurements. This work was support by a PhD grant from the French Ministère de l'Enseignement Supérieur et de la Recherche.

References

- [1] M. Tomaszekiewicz, M. Abou Najm, D. Beysens, I. Alameddine, M. El-Fadel, Dew as a sustainable non-conventional water resource: a critical review, *Environmental Reviews* 23 (4) (2015) 425–442. doi:10.1139/er-2015-0035.
- [2] D. Beysens, *Dew Water*, River Publishers, Gistrup, 2018.
- [3] J. Monteith, M. Unsworth, *Principles of Environmental Physics: Plants, Animals, and the Atmosphere*, Elsevier Science, 2013.
- [4] T. Nilsson, W. Vargas, G. Niklasson, C. Granqvist, Condensation of water by radiative cooling, *Renewable Energy* 5 (1-4) (1994) 310–317. doi:10.1016/0960-1481(94)90388-3.
- [5] O. Clus, I. Lekouch, M. Muselli, I. Milimouk-Melnitchouk, D. Beysens, Dew, fog and rain water collectors in a village of s-morocco (idouakssou), *Desalination and Water Treatment* 51 (2013) 4235–4238. doi:10.1080/19443994.2013.768323.
- [6] D. Beysens, A. Mongruel, K. Acker, Urban dew and rain in paris, france : Occurence and physico-chemical characteristics, *Atmospheric research* 189 (2017) 152–161. doi:10.1016/j.atmosres.2017.01.013.

- [7] G. Sharan, A. Roy, L. Royon, A. Mongrue, D. Beysens, Dew plant for bottling water., *Journal of Cleaner Production* 155 (2016) 83–92. doi:10.1016/j.jclepro.2016.07.079.
- [8] K. R. Scott, Use of liquid nitrogen in a winterhardiness test chamber for fruit trees, *Canadian Journal of Plant Science* 46 (6) (1966) 691–693. doi:10.4141/cjps66-116.
- [9] A. R. Aston, R. J. Millington, D. B. Peters, Radiation exchange in controlling leaf temperature, *Agronomy Journal* 61 (5) (1969) 797–800. doi:10.2134/agronj1969.00021962006100050044x.
- [10] J. Aston, D. Paton, Frost room design for radiation frost studies in eucalyptus, *Australian Journal of Botany* 21 (2) (1973) 193–199. doi:10.1071/BT9730193.
- [11] P. A. Gill, P. D. Waister, Design and Performance of a Portable Frost Chamber for the Investigation of Hardiness of Strawberries, *Journal of Horticultural Science* 51 (4) (1976) 509–513. doi:10.1080/00221589.1976.11514720.
- [12] B. C. Clifford, The construction and operation of a dew-simulation chamber, *New Phytologist* 72 (3) (1973) 619–623. doi:10.1111/j.1469-8137.1973.tb04411.x.
- [13] D. Pescod, A method of forming dew on plants under controlled conditions, *Journal of Agricultural Engineering Research* 10 (4) (1965) 328–332. doi:10.1016/0021-8634(65)90079-X.
- [14] F. W. Went, V. R. Babu, The Effect of Dew on Plant Water Balance in *Citrullus vulgaris* and *Cucumis melo*, *Physiologia Plantarum* 44 (3) (1978) 307–311. doi:10.1111/j.1399-3054.1978.tb08637.x.
- [15] H. Marcellos, A plant freezing chamber with radiative and convective energy exchange, *Journal of Agricultural Engineering Research* 26 (5) (1981) 403–408. doi:10.1016/0021-8634(81)90116-5.

- [16] D. Flura, B. Itier, O. Brun, B. Durand, S. Masson, Mise au point de chambres de refroidissement pour l'étude de la gélivité des bourgeons. application au cas de la vigne, *Agronomie* 11 (5) (1991) 383–386. doi:10.1051/agro:19910505.
- [17] M. P. Fuller, P. L. Grice, A chamber for the simulation of radiation freezing of plants, *Annals of Applied Biology* 133 (1) (1998) 111–121. doi:10.1111/j.1744-7348.1998.tb05807.x.
- [18] B. Kotzen, Innovation and evolution of forms and materials for maximising dew collection, *Ecocycles* 1 (1) (2015) 39–50. doi:10.19040/ecocycles.v1i1.33.
- [19] L. Zhou, H. Song, J. Liang, M. Singer, M. Zhou, E. Stegenburgs, N. Zhang, C. Xu, C. Ng, Z. Yu, B. Ooi, Q. Gan, A polydimethylsiloxane-coated metal structure for all-day radiative cooling., *Nature Sustainability* 2 (2019) 718–724. doi:10.1038/s41893-019-0348-5.
- [20] M. Hori, T. Aoki, T. Tanikawa, H. Motoyoshi, A. Hachikubo, K. Sugiura, T. J. Yasunari, H. Eide, R. Stordvold, Y. Nakajima, F. Takahashi, In-situ measured spectral directional emissivity of snow and ice in the 8-14 μm atmospheric window, *Remote Sensing of Environment* 100 (4) (2006) 486–502. doi:10.1016/j.rse.2005.11.001.
- [21] M. Lawrence, The relationship between relative humidity and the dewpoint temperature in moist air : a simple conversion and applications, *Bull. Amer. Meteor. Soc.* 86 (2) (2005) 225–234. doi:10.1175/BAMS-86-2-225.
- [22] S. Anand, K. Rykaczewski, S. Subramanyam, D. Beysens, K. Varanasi, How droplets nucleate and grow on liquids and liquid impregnated surfaces, *Soft Matter* 11 (2015) 69–80. doi:10.1039/c4sm01424c.
- [23] W. Minkina, D. Klecha, Atmospheric transmission coefficient modelling in the infrared for thermovision measurements, *Journal of Sensors and Sensor System* 5 (2016) 17–23. doi:10.5194/jsss-5-17-2016.

- [24] B. Wiecek, Thermovision in infrared – basics and applications (in Polish), Measurement Automation Monitoring Publishing House, 2011.
- [25] R. J. Bliss, Atmospheric radiation near the surface of the ground : a summary for engineers, *Solar Energy* 5 (3) (1961) 103–120. doi:10.1016/0038-092X(61)90053-6.
- [26] A. Gustavsen, P. Berdahl, Spectral emissivity of anodized aluminium and the thermal transmittance of aluminium window frames, *Nordic Journal of Building Physics* 3 (2003) 1–12.
- [27] D. Salmon, Thermal conductivity of insulations using guarded hot plates, including recent developments and sources of reference materials, *Measurement Science and Technology* 12 (2001) R89–R98. doi:10.1088/0957-0233/12/12/201.
- [28] D. Lide, CRC Handbook of Chemistry and Physics, 79th Edition, Taylor & Francis, 1998.
- [29] R. J. Goldstein, K.-S. Lau, Laminar natural convection from a horizontal plate and the influence of plate-edge extensions, *Journal of Fluid Mechanics* 129 (1983) 55–75. doi:10.1017/S0022112083000646.
- [30] E. Radziemska, W. Lewandowski, Heat transfer by natural convection from an isothermal downward-facing round plate in unlimited space, *Applied Energy* 68 (4) (2001) 347–366. doi:10.1016/S0306-2619(00)00061-1.
- [31] S. W. Churchill, H. H. Chu, Correlating equations for laminar and turbulent free convection from a vertical plate, *International Journal of Heat and Mass Transfer* 18 (11) (1975) 1323–1329. doi:10.1016/0017-9310(75)90243-4.
- [32] M. Huetz-Aubert, S. Karlsfeld, P. De Dianous, Rayonnement thermique des matériaux semi-transparents, *Techniques de l'ingénieur. Génie énergétique* 2:B8215 v1 (1995).

- [33] J. Trosseille, A. Mongruel, L. Royon, M.-G. Medici, D. Beysens, Roughness-enhanced collection of condensed droplets, *The European Physical Journal E* 42 (144) (2019). doi:10.1140/epje/i2019-11905-9.
- [34] G. Linteris, M. Zammarano, B. Wilthan, L. Hanssen, Absorption and reflection of infrared radiation by polymers in fire-like environments, *Fire and Materials* 36 (7) (2012) 537–553. doi:10.1002/fam.1113.
- [35] M.-G. Medici, A. Mongruel, L. Royon, D. Beysens, Edge effects on water droplet condensation, *Physical Review E* 90 (6) (2014) 062403. doi:10.1103/PhysRevE.90.062403.
- [36] B. Suleiman, J. Larfeldt, B. Leckner, M. Gustavsson, Thermal conductivity and diffusivity of wood, *Wood Science and Technology* 33 (1999) 465–473. doi:10.1007/s002260050130.
- [37] S. Churchill, H. Chu, Correlating equations for laminar and turbulent free convection from a horizontal cylinder, *Int. J. Heat Mass Transfer* 18 (1975) 1049–1063. doi:10.1016/0017-9310(75)90222-7.
- [38] T. Bergman, A. Lavine, F. Incropera, D. DeWitt, *Fundamentals of Heat and Mass Transfer*, 7th Edition, John Wiley and Sons, 2011.
- [39] D. Zhao, A. Aili, Y. Zhai, S. Xu, G. Tan, X. Yin, R. Yang, Radiative sky cooling : Fundamental principles, materials and applications., *Appl. Phys. Rev.* 6 (2019) 021306. doi:10.1063/1.5087281.
- [40] D. Beysens, M. Muselli, I. Milimouk, C. Ohayon, B. S., E. Soyeux, M. Mileta, P. Ortega, Application of passive radiative cooling for dew condensation, *Energy* 31 (2006) 2303–2315. doi:10.1016/j.energy.2006.01.006.
- [41] H. D. Downing, D. Williams, Optical constants of water in the infrared, *Journal of Geophysical Research* 80 (12) (1975) 1656–1661. doi:10.1029/JC080i012p01656.

- [42] H. Zhao, D. Beysens, From Droplet Growth to Film Growth on a Heterogeneous Surface: Condensation Associated with a Wettability Gradient, *Langmuir* 11 (2) (1995) 627–634. doi:10.1021/1a00002a045.

Graphical Abstract

Radiative cooling for dew condensation

Joachim Trosseille, Anne Mongruel, Laurent Royon, Daniel Beysens

